Exciton in phosphorene: Strain, impurity, thickness, and heterostructure

Srilatha Arra,[1,*] Rohit Babar,[2,*] and Mukul Kabir[2,3,†]

[1]*Department of Chemistry, Indian Institute of Science Education and Research, Pune 411008, India*

[2]*Department of Physics, Indian Institute of Science Education and Research, Pune 411008, India*

[3]*Centre for Energy Science, Indian Institute of Science Education and Research, Pune 411008, India*

(Received 31 October 2018; published 22 January 2019)

Reduced electron screening in two dimensions plays a fundamental role in determining exciton properties, which dictates optoelectronic and photonic device performances. Considering the explicit electron-hole interaction within the GW plus Bethe-Salpeter equation (BSE) formalism, we first study the excitonic properties of pristine phosphorene and investigate the effects of strain and impurity coverage. The calculations reveal strongly bound excitons in these systems with anisotropic spatial delocalization. Further, we present a simplified hydrogenic model with anisotropic exciton mass and effective electron screening as parameters, and the corresponding results are in excellent agreement with the present GW-BSE calculations. The simplified model is then used to investigate exciton renormalization in few-layer and heterostructure phosphorene. The changes in carrier effective mass along with increasing electron screening renormalize the exciton binding in these systems. We establish that the present model, in which the parameters are calculated within computationally less expensive first-principles calculations, can predict exciton properties with excellent accuracy for larger two-dimensional systems, for which the many-body GW-BSE calculations are impossible.

DOI: 10.1103/PhysRevB.99.045432

I. INTRODUCTION

Excitonic properties in reduced dimensions are markedly different due to the fundamental difference in electron screening and have attracted much attention conceptually in recent times [1–6]. Weaker electron screening in one-dimensional systems, such as carbon and boron nitride nanotubes, results in high exciton binding [1–3]. Likewise, the two-dimensional (2D) materials interact strongly with light, and the concurrently generated electron-hole pairs interact strongly due to reduced screening [7–12]. For example, while exciton binding is small, 84 meV, in bulk MoS_2 [13], due to reduced screening in monolayer MoS_2, it is measured to be in the 220–570 meV range [9–11]. Moreover, unlike the Frenkel excitons, the excitons in 2D materials can be delocalized in space and extend over 1 nm [8,12,14]. Further, the widely varying exciton binding has been reported in a different class of materials and has important implications in device applications. For applications in solar cells, photodetectors, and catalytic devices, an exciton with weak binding leading to easy dissociation is desirable. In contrast, materials with strong exciton binding are ideal to study plausible exciton-polariton condensates and for applications such as polariton lasing [15].

Phosphorene has attracted a lot of attention due to its many plausible technological applications [16–20] and has become an interesting proving ground for many-body physics [21–23]. The Dirac semimetal state has been experimentally realized in few-layer phosphorene under adatom absorption [22]. We have recently reported an intrinsic, robust, and high-temperature Kondo state in defect-containing phosphorene doped with a transition-metal impurity [23]. In the present context, phosphorene has unique optical properties that are mainly determined by the quasiparticle band structure and screening. Originating from a puckered honeycomb network, the electronic band structure is highly asymmetric in phosphorene, and consequently, the optical properties are also found to be highly anisotropic [4,17,18,24]. The quasiparticle and optical gaps of single-layer phosphorene (SLP) are experimentally measured to be 2.2 ± 0.1 and 1.3 ± 0.02 eV, respectively, through photoluminescence excitation spectroscopy [24]. This results in a very high exciton binding energy of 0.9 ± 0.12 eV due to reduced screening in 2D quantum confinement.

Studying quasiparticle band structure and the corresponding optical properties is a nontrivial and computationally expensive task. The conventional density functional approach fails to reproduce the correct experimental results which involve excited states [25]. In contrast, the many-body perturbation-theory-based GW method produces the correct quasiparticle energies [26]. In this approach, the electron self-energies are expressed in terms of Green's function G and screened Coulomb interaction W. Further, the optical properties of semiconductors and insulators are strongly affected by interacting electron-hole pairs, which are described through the Bethe-Salpeter equation (BSE) [27–29]. These theoretical descriptions lead to excellent agreement with the experimental results [25].

Here, we study the quasiparticle and optical properties of SLP and its derivatives within the GW and BSE formalisms and also investigate the effects of strain. Results for the pristine SLP are in excellent agreement with those obtained from the transmission and photoluminescence

*These authors contributed equally to this work.

†Corresponding author: mukul.kabir@iiserpune.ac.in

spectroscopies [24,30]. The optical absorption and the corresponding excitons are found to be highly anisotropic. Due to the 2D confinement of photogenerated electron-hole pairs, the exciton binding is exceptionally strong, which is in accordance with the experimental measurements [24].

While a rigorous treatment of electron-hole interaction within the BSE formalism provides an excellent description of exciton binding [12,14,25,31,32], it is computationally very expensive and thus restricted to systems that are small in size. In this context and following earlier attempts [33,34], we describe a hydrogenic effective exciton mass model in which the parameters, the effective carrier masses and the static dielectric constant, are calculated within the conventional density functional theory (DFT) calculations. The results of this simplified model are in excellent agreement with those calculated within the BSE formalism for the pristine and strained SLPs along with the SLPs with one-monolayer (1-ML) impurity coverage. Further, the anisotropic hydrogenic model is extended for larger systems with low impurity coverages that were previously predicted to be good candidate materials for water redox reactions [20].

The quantum confinement of excitons should be extraordinarily affected by varying thickness of the 2D material, which alters electron screening. This picture is well captured within the present model through the renormalization of exciton binding in few-layer phosphorene. Furthermore, the practical applications of phosphorene are limited due to its fast degradation in ambient conditions, resulting in a severe alteration in the corresponding electronic properties [35–37]. Thus, to avoid degradation, phosphorene is encapsulated with a capping layer and substrate, and the devices restore the intrinsic carrier mobility of phosphorene [16,24,35,38–40]. In this regard, we investigate the electronic and exciton properties in SLP encapsulated with atomically thin hexagonal boron nitride (h-BN), which is often used to protect phosphorene from degradation [38–40].

II. METHODOLOGY

The structural optimizations were carried out within the conventional DFT formalism as implemented in the VASP code [41,42], where the electrons are treated within the projector augmented-wave method [43]. The Kohn-Sham orbitals were expanded in a plane-wave basis with a 400 eV energy cutoff. The exchange-correlation energy was described with the Perdew-Burke-Ernzerhof (PBE) functional [44]. The Brillouin zone was sampled using a Γ-centered $17 \times 13 \times 1$ Monkhorst-Pack k grid [45]. Complete structural optimization was carried out until the forces exerted on each atom were less than a 0.01 eV/Å threshold. In phosphorene, three electrons participate in the covalent σ bonding with three neighboring P atoms, whereas the remaining two electrons occupy a lone pair orbital. Thus, for phosphorene and its derivatives such as P_4X (X=O and S), we considered van der Waals (vdW) interaction through the nonlocal correlation functional optB88-vdW during the structural optimization [46,47], while for the larger systems in few-layer and heterostructure phosphorene we used the D3 functional with zero damping [48]. The obtained lattice parameters for SLP are $a = 4.58$ and $b = 3.32$ Å along the armchair and zigzag directions, respectively, and are consistent with previous reports and experimental black phosphorus (see the Supplemental Material) [30,35,49–52].

The optimized structures with the PBE exchange-correlation functional are then used for the subsequent GW-BSE calculations. The quasiparticle (QP) picture is investigated within the partially self-consistent GW_0 approach by iterating the one-electron energies in the Green's function G [26,53]. Two self-consistent updates for the Green's function (G_2W_0) are found to be sufficient to converge the QP band gap. The convergence of the QP gap as a function of unoccupied bands was found to be much faster for phosphorene [4], and we find 158 such bands to be sufficient in this regard. Further, the electron-hole interactions are incorporated within the BSE formalism, which provides the optical gap and the corresponding exciton binding energy [25,28,29].

The optical properties are calculated using a frequency-dependent complex dielectric tensor, $\varepsilon(\omega) = \varepsilon'(\omega) + i\varepsilon''(\omega)$. The imaginary part $\varepsilon''(\omega)$ of the linear dielectric tensor is calculated in the long-wavelength $\mathbf{q} \to \mathbf{0}$ limit [54],

$$\varepsilon''_{\alpha\beta}(\omega) = \frac{4\pi^2 e^2}{\Omega} \lim_{q\to 0} \frac{1}{q^2} \sum_{c,v,\mathbf{k}} 2w_{\mathbf{k}} \delta(\epsilon_{c\mathbf{k}} - \epsilon_{v\mathbf{k}} - \omega) \times \langle u_{c\mathbf{k}+\mathbf{e}_\alpha q} | u_{v\mathbf{k}} \rangle \langle u_{c\mathbf{k}+\mathbf{e}_\beta q} | u_{v\mathbf{k}} \rangle^*, \quad (1)$$

where Ω is the volume of the primitive cell, $\omega_{\mathbf{k}}$ are k-point weights, and the factor of 2 inside the summation accounts for the spin degeneracy. The $\epsilon_{c\mathbf{k}}$ ($\epsilon_{v\mathbf{k}}$) are $\mathbf{k}$-dependent conduction (valence) band energies, $u_{c\mathbf{k},v\mathbf{k}}$ are the cell-periodic parts of the pseudo-wave-function, and $\mathbf{e}_{\alpha,\beta}$ are unit vectors along the Cartesian directions. The real part $\varepsilon'(\omega)$ is calculated using the Kramers-Kronig transformation, and the absorption coefficient is calculated as $\Lambda_{\alpha\alpha}(\omega) = \frac{2\omega}{c}[|\varepsilon_{\alpha\alpha}(\omega)| - \varepsilon'_{\alpha\alpha}(\omega)]^{\frac{1}{2}}$.

The BSE calculations were carried out using the VASP code [41,42], and for completeness, we briefly describe the formalism. Within the BSE, an exciton state $|S\rangle$ can be written as [29]

$$|S\rangle = \sum_{\mathbf{k}} \sum_{v}^{\text{hole}} \sum_{c}^{\text{elec}} A^S_{vc\mathbf{k}} |vc\mathbf{k}\rangle, \quad (2)$$

where $|vc\mathbf{k}\rangle = \hat{a}^\dagger_{v\mathbf{k}} \hat{b}^\dagger_{c\mathbf{k}+\mathbf{q}} |0\rangle$, with $|0\rangle$ being the ground state, and $\hat{a}^\dagger$ ($\hat{b}^\dagger$) is hole (electron) creation operator. Here, $\mathbf{q}$ is the momentum of the absorbed photon, and $A^S_{vc\mathbf{k}}$ are electron-hole amplitudes. The corresponding excitation energies E_S are determined via BSE [55],

$$\left(\epsilon^{\text{QP}}_{c\mathbf{k}+\mathbf{q}} - \epsilon^{\text{QP}}_{v\mathbf{k}}\right) A^S_{vc\mathbf{k}} + \sum_{v'c'\mathbf{k}'} A^S_{v'c'\mathbf{k}'} \langle vc\mathbf{k}|K^{eh}|v'c'\mathbf{k}'\rangle = E_S A^S_{vc\mathbf{k}}, \quad (3)$$

where ϵ^{QP} are quasiparticle energies and K^{eh} is the electron-hole interaction. The imaginary part of the dielectric function $\varepsilon''(\omega)$ is calculated with the optical transition matrix element of the excitations.

Such a rigorous treatment within the many-body theory coupled with the BSE scheme provides an excellent description of QP and optical gaps and exciton binding, which all compare well with the experimental results [12,14,25,31,32]. However, such a treatment is restricted to the systems that are small in size due to its exceptional computational cost. Thus,

one needs to develop simplified models to investigate excitons in realistic systems with appreciable accuracy. For three-dimensional materials, the simplistic Mott-Wannier model predicts the exciton binding energy as $E_x^{3D} = (\mu/\varepsilon^2)R_\infty$, where R_∞ is the Rydberg constant. The excitonic effective mass μ and the static dielectric constant ε can easily be calculated within the standard electronic structure calculations [56].

In contrast, the excitonic properties of two-dimensional materials are fundamentally different from their 3D counterpart and cannot be described within the Mott-Wannier approach. In 2D materials, excitons are strongly confined, and the dielectric screening is considerably reduced [7–12]. There have been recent efforts to develop excitonic models for 2D materials; however, a significant effort has been devoted to isotropic materials such as transition-metal dichalcogenides [6,33,34,57,58]. Here, we present a generalized scheme appropriate for anisotropic electronic materials such as phosphorene and its various derivatives [33,34].

For 2D semiconducting systems, the effective exciton Hamiltonian can be written as

$$H_x = -\hbar^2 \frac{\nabla_r^2}{2\mu} + V_{2D}(r), \tag{4}$$

where $\mu^{-1} = m_e^{-1} + m_h^{-1}$ is the exciton reduced mass and r is the electron-hole separation. Following Keldysh, the nonlocally screened electron-hole interaction is described by [59]

$$V_{2D}(r) = -\frac{e^2}{4(\varepsilon_1+\varepsilon_2)\varepsilon_0 r_0}\left[H_0\left(\frac{r}{r_0}\right) - Y_0\left(\frac{r}{r_0}\right)\right], \tag{5}$$

where ε_1 and ε_2 are the dielectric constants of the upper and lower media and ε_0 is the vacuum permittivity. H_0 and Y_0 are Struve and Bessel functions. The screening length r_0 is related to the 2D polarizability χ_{2D} as $r_0 = 2\pi\chi_{2D}$ [60], where χ_{2D} is calculated using the static dielectric constant ε of the concerned 2D material, $\varepsilon(L_v) = 1 + 4\pi\chi_{2D}/L_v$, where L_v is the transverse vacuum size. The ε is calculated from the real part of the complex dielectric tensor $\varepsilon(\omega)$ at zero frequency. Note that the interaction V_{2D} at large separation $r \gg r_0$ follows the $1/r$ Coulomb interaction, whereas at the $r \ll r_0$ limit, the interaction reduces to a weaker $\ln(r)$ dependence.

The variational excitonic wave function for an anisotropic electronic material such as phosphorene with $m_e^x \neq m_e^y$ and $m_h^x \neq m_h^y$ was proposed previously [33,34] and is written as

$$\psi(x,y) = 2\sqrt{\frac{2}{\pi\lambda a_x^2}}\exp\left[-\{(x/a_x)^2 + (y/a_y)^2\}^{\frac{1}{2}}\right], \tag{6}$$

where $a_y = \lambda a_x$ is the anisotropic exciton extension along the x (armchair) and y (zigzag) directions and is treated as a variational parameter. Using this form of excitonic wave function $\psi(x,y)$, the expectation value of the kinetic energy is calculated to be [33]

$$E_k(\lambda, a_x) = \frac{\hbar^2}{4a_x^2}\left[\frac{1}{\mu_x} + \frac{1}{\lambda^2\mu_y}\right]. \tag{7}$$

Here, μ_x and μ_y are the reduced exciton masses along the x and y directions, respectively. The corresponding potential energy is given by [33]

$$E_p(\lambda, a_x) = \int\int V_{2D}(x,y)|\psi(x,y)|^2 dxdy. \tag{8}$$

The variational exciton binding energy, $E_x^{2D}(\lambda, a_x) = E_k(\lambda, a_x) + E_p(\lambda, a_x)$, is minimized with respect to the variational parameters λ and a_x to obtain the exciton binding energy and (anisotropic) exciton extension. The parameters in the above model, effective electron and hole masses in different crystallographic directions and the static dielectric constant, are then calculated from the first-principles calculations. In principle, these parameters can be calculated using any level of approximation to the exchange-correlation functional, and here, we have used the Heyd-Scuseria-Ernzerhof (HSE06) hybrid functional [61,62].

III. RESULTS AND DISCUSSION

First, we discuss the optical and excitonic properties of pristine phosphorene and investigate the effect of uniaxial strain along the different crystallographic directions. Here, we compare the computationally expensive GW-BSE results for these systems with the simplified model calculations. Once we demonstrate excellent agreement between these methods, we extend our investigation within the simplified model for realistically large systems, for which GW-BSE calculations are practically impossible.

A. Pristine phosphorene

We start with the electronic and optical properties of single-layer pristine phosphorene [Fig. 1(a)] within the GW-BSE approach. Due to the long-range Coulomb interactions, these properties of 2D materials are strongly influenced by the vertical separation L_z between the periodic images [2,4]. As it was shown earlier that the QP band gap converges as $1/L_z$, we extrapolate the gap to the $L_z \to \infty$ limit, which we found to be 2.14 eV [Fig. 1(b) and Table I]. This extrapolated E_g^{QP} is in excellent agreement with the previous theoretical results [4] and with the two experimental results that are available to date [24,30]. High-resolution transmission spectroscopy predicted a transport gap of 2.05 eV [30], while photoluminescence excitation spectroscopy suggested a QP gap of 2.2 ± 0.1 eV [24]. In comparison, the earlier G_0W_0 results vary between 1.60 and 2 eV [63,64]. The present $L_z \to \infty$ interpolated QP gaps are much smaller, 1.79 (G_1W_0) and 1.75 eV (G_1W_1), than the G_2W_0 gap. Thus, we argue that the self-consistent correction to the self-energy ($\Sigma = iGW$), through the Green's function update, is essential to predict the QP gap correctly [4]. It is important to note here that the optical gap converges much faster than the QP gap with varying L_z [Fig. 1(b)].

The absorption coefficient $\Lambda(\omega)$ calculated without and with the electron-hole interaction shows strong anisotropy for the light polarizations along the armchair and zigzag directions [Figs. 1(c) and 1(d)]. The $L_z \to \infty$ extrapolated optical gap of 1.40 eV [Fig. 1(b) and Table I] along the armchair direction is in excellent agreement with the experimental range of 1.30–1.45 eV [17,24]. The large exciton binding energy of 0.74 eV indicates a strongly bound exciton in SLP, which is in

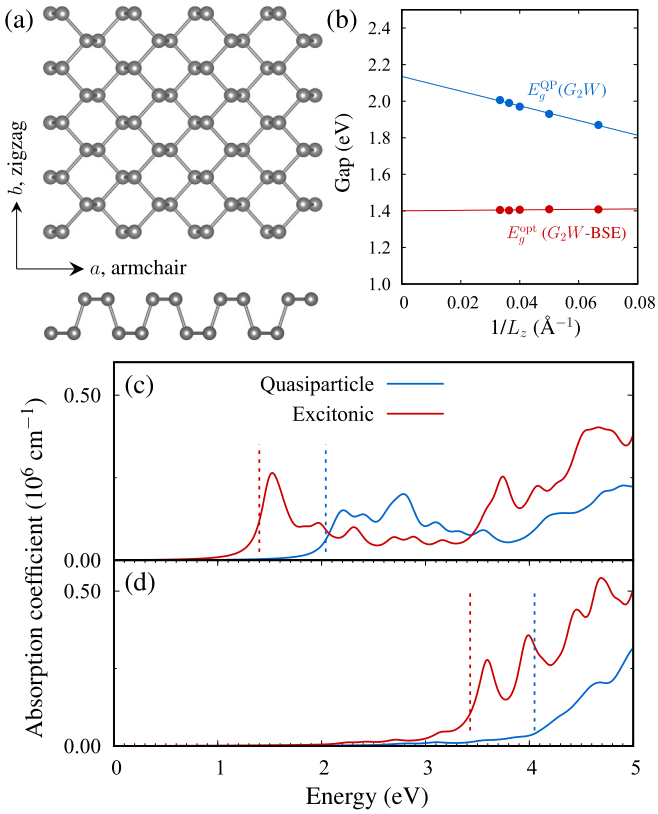

FIG. 1. (a) The top and side views of single-layer phosphorene are shown, indicating the armchair and zigzag crystallographic directions. (b) The QP and optical gaps are calculated with varying vertical separation L_z between the layers and extrapolated to $L_z \to \infty$. The results are in excellent agreement with the experimental results [17,24,30]. Absorption coefficient calculated without and with the electron-hole interaction for $L_z = 30$ Å. $\Lambda(\omega)$ shows strong absorption anisotropy between the light polarization along the (c) armchair and (d) zigzag directions. The vertical lines indicate the band edges corresponding to the first absorption peak. The energy difference between the QP and optical gaps indicates a strongly bound exciton.

excellent agreement with the previous GW-BSE calculations [4,64] and the experimental prediction of 0.9 ± 0.12 eV [24]. Note the absorption edge corresponding to light absorption along the zigzag crystallographic direction lies at a much higher energy, and thus, SLP shows linear dichroism [49].

We calculate the exciton binding within the hydrogenic effective exciton mass model, in which the parameters are calculated from a relatively less computationally expensive treatment of the electron exchange and correlation, namely, within the HSE06 hybrid functional. The effective carrier masses are highly anisotropic (Table I), as estimated by fitting the HSE06 bands to the parabolic dispersion $E(k) = \hbar^2 k^2/2m^*$. The estimated m_e^* is much smaller ($0.16m_e$) along the armchair direction than along the zigzag direction ($1.40m_e$), where m_e is the electron rest mass. The qualitative picture is the same for the hole, as m_h^* along the armchair direction is much lighter ($0.12m_e$) than the $4.69m_e$ along the zigzag direction. Thus, the effective exciton mass along the armchair direction is much lighter than that along the zigzag direction ($\mu_x \ll \mu_y$). These results are in good agreement with the previous results [49,65]. The other parameter of the model, the static dielectric constant, is calculated from the real part of the complex dielectric function at zero frequency. The average of the static ε along the armchair and zigzag directions is used to calculate the 2D polarizability χ_{2D} (Table I). Using these parameters, the effective exciton mass model predicts an exciton binding energy of 0.79 eV, which is in excellent agreement with the present GW-BSE prediction and the experimental estimations (Table I) and is also consistent with the earlier estimation [33].

The spatial distribution of excitons in the ground state is found to be anisotropic and extended along the armchair direction ($a_x = 12.26$ and $a_y = 4.90$ Å), with spatial anisotropy satisfying the relation $\lambda = a_y/a_x \sim (\mu_x/\mu_y)^{1/3}$, which was analytically predicted previously [33]. In agreement, such an elliptic spatial structure of bound holes has recently been observed in black phosphorus through scanning tunneling microscope tomographic imaging [66].

B. Effect of uniaxial strain

The effect of uniaxial strain on the electronic structure of SLP was studied previously within the conventional exchange-correlation functional [23,65,67,68]. However, the considerations of self-energy correction and electron-hole interaction are scarce in this regard. Here, we investigate the QP and optical gaps and the corresponding exciton binding for SLP under $\varepsilon_s^{a/z} = \pm 5\%$ uniaxial strain [Table I and Figs. 2(a) and 2(b)], while the strained lattice is relaxed along the transverse direction. We previously reported that the strain energy along the zigzag direction is much higher than that along the armchair direction, and thus, straining the SLP along the armchair direction is comparatively easier [23]. Within the $-5\% \le \varepsilon_s^{a/z} \le +5\%$ strain range, the $L_z \to \infty$ interpolated gaps E_g^{QP} and E_g^{opt} decrease with uniaxial compressive strain, while they increase with tensile strain (Table I). Clearly, the many-body interaction is comparatively more affected by the uniaxial strain along the armchair direction. Further, the compressive strain triggers a stronger gap renormalization than a tensile strain of equal magnitude. The absorption anisotropy in different crystallographic directions remains intact [Fig. 2(a)]. Within the applied strain range, the first absorption peak appears within 1–1.50 eV for light polarization along the armchair direction. In contrast, for light polarization along the zigzag direction, the first peak appears above 3 eV and, in general, shows higher absorbance. Applied uniaxial strain changes the oscillator strength significantly [Fig. 2(a)]. While the oscillator strength corresponding to the ground-state exciton changes by $\pm 10\%$ for $\varepsilon_s^a = \pm 5\%$ strain along the armchair direction, the change is even more significant, $\mp 30\%$, for applied strain $\varepsilon_s^z = \pm 5\%$ along the zigzag direction. Interestingly, for $\varepsilon_s^z = 5\%$, we observe a competing absorption peak just below its QP gap. Such strain-dependent E_g^{QP} and E_g^{opt} may explain the variation observed in the photoluminescence peak on different substrates [17,24].

The excitons remain strongly bound under applied strain, and the G_2W_0-BSE calculated E_x varies between 700 and 900 meV within the investigated strain range. The subsequent excited states reflect a sensitive dependence on the strain-dependent dielectric screening [Fig. 2(b)]. Thus, strain

TABLE I. With varying L_z, the quasiparticle E_g^{QP} and optical E_g^{opt} gaps are calculated within the G_2W_0 and G_2W_0-BSE approaches, respectively, which are subsequently interpolated to $L_z \to \infty$. The parameters for the simplified exciton model, the effective carrier masses m_e^* and m_h^* along the armchair and zigzag directions, and the average static dielectric constant are calculated within the HSE06 hybrid functional. The corresponding 2D polarizability χ_{2D} is also tabulated. The uniaxial strain severely affects the many-body interaction in phosphorene, and thus, E_g^{QP}, E_g^{opt}, and E_{x} are altered. The effect of high impurity coverage is also investigated. The exciton binding energies E_{x} calculated within the hydrogenic exciton model compare excellently with those from the accurate, but computationally expensive, GW-BSE formalism and available experimental results.

	E_g^{QP}	E_g^{opt}	E_{x} (eV)		Armchair (x)		Zigzag (y)			χ_{2D}
System	(eV)	(eV)	BSE	model	m_e^*/m_e	m_h^*/m_e	m_e^*/m_e	m_h^*/m_e	ε	(Å)
SLP,	2.05 [30]	1.45 [17]								
experiment	2.2 ± 0.1 [24]	1.30 [24]	0.9 ± 0.12 [24]							
SLP, $L_z \to \infty$	2.14	1.40	0.74	0.79	0.16	0.12	1.40	4.69	2.60	3.55
SLP, $\varepsilon_s^a = -5\%$	1.78	1.03	0.75	0.72	0.14	0.12	1.35	3.10	2.78	3.95
SLP, $\varepsilon_s^a = +5\%$	2.38	1.51	0.87	0.80	0.13	0.12	1.45	3.28	2.51	3.36
SLP, $\varepsilon_s^z = -5\%$	1.89	1.12	0.77	0.78	0.23	0.13	1.39	2.64	2.70	3.77
SLP, $\varepsilon_s^z = +5\%$	2.20	1.41	0.79	0.78	0.20	0.14	1.39	2.76	2.71	3.79
P_4O	3.22	2.31	0.91	0.81	0.76	0.24	0.17	3.42	2.48	3.17
P_4S	2.74	1.87	0.87	0.67	0.63	0.24	0.80	0.40	3.19	4.63

engineering in phosphorene leads to widely tunable photoluminescence energy, enhanced absorption, and multiple-exciton formation.

Next, we investigate the effective carrier masses with a varied uniaxial strain within the HSE06 functional. In agreement with an earlier report [65], the effective electron and hole masses are severely affected by strain (Table I); however, their qualitative anisotropic nature remains intact with $\mu_x \ll \mu_y$. These m_e^* and m_h^* are used to estimate E_{x} for the strained SLP within the hydrogenic model, which are in excellent agreement with the more accurate GW-BSE results (Table I). Further, the spatial anisotropy of excitons $\lambda \sim (\mu_x/\mu_y)^{1/3}$ under strain remains similar to that in pristine SLP (see the Supplemental Material) [52]. These results essentially validate the applicability of the present hydrogenic model anisotropic 2D phosphorene.

C. Effect of impurity coverage

The presence of lone-pair electrons in phosphorene makes it reactive, and it can easily absorb impurities with a strong binding energy resulting from the P to impurity charge transfer. We previously discussed O, S, and N chemisorption with varied impurity coverage, and we concluded that 0.25–0.5-ML O/S coverages become conducive to both water redox reactions [20]. While the exciton binding energy plays an important role in efficient charge separation and in turn affects the performance of a catalytic device, the SLP derivatives with such low impurity coverages are very difficult to

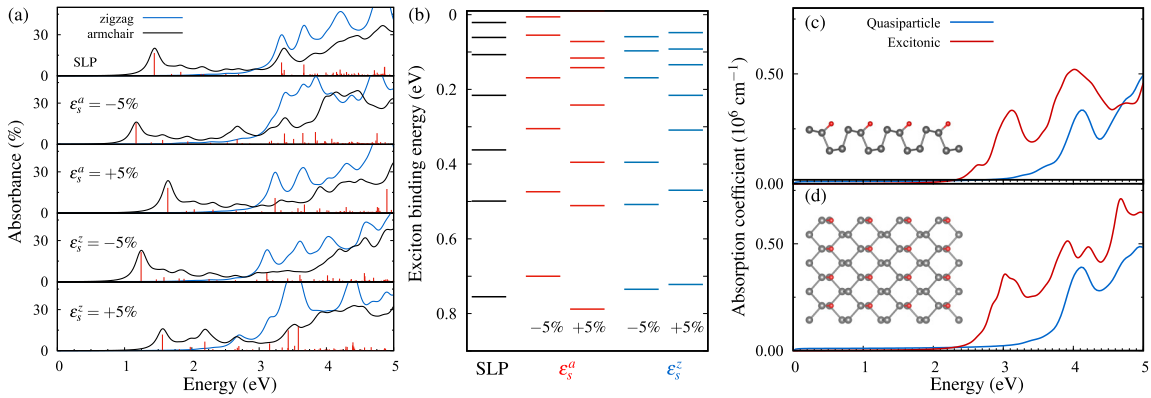

FIG. 2. (a) The effects of strain on the absorbance and dipole oscillator strength calculated including the electron-hole interaction within the GW-BSE formalism ($L_z = 30$ Å). The vertical lines indicate the relative dipole oscillator strengths and are significantly affected by the applied uniaxial strain. (b) The corresponding exciton spectra for the pristine and uniaxially strained SLP. Strain-dependent dielectric screening influences the spectra. $E = 0$ eV refers to the quasiparticle gap, and excitons generated from the transitions with the nonvanishing dipole oscillator strengths are shown. The relative oscillator strengths are shown in (a). Absorption coefficient calculated without and with the electron-hole interaction ($L_z = 30$ Å) for the light polarization along (c) the armchair and (d) zigzag directions, shown for 1-ML O coverage. The absorption edges are calculated from the corresponding E vs $(E\Lambda)^{1/2}$ plot for this indirect gap semiconductor. The absorption anisotropy along the armchair and zigzag directions is greatly reduced due to monolayer impurity coverage. The insets show the side and top views of SLP with 1-ML O coverage.

investigate within the GW-BSE formalism. Thus, first, we investigate the derivatives with high 1-ML O/S coverages, P_4O and P_4S, which can be represented by a small cell, and compare the GW-BSE results with the effective mass model.

The SLPs with 1-ML O and S coverage are found to be indirect gap semiconductors, and both QP and optical gaps are severely altered (Table I). While for the 1-ML O-covered SLP the extrapolated E_g^{QP} and E_g^{opt} increase upon impurity coverage, the picture is reversed for the 1-ML S-covered SLP. The absorption edge, calculated by considering the electron-hole interaction, lies at a much lower energy than that calculated without the interaction (Fig. 2). This observation indicates strongly bound excitons in these derivatives similar to the pristine SLP (Table I). The qualitative anisotropic feature in the carrier effective masses is intact but is severely altered in all crystallographic directions [52]. However, the anisotropy in the effective exciton mass disappears with $\lambda \sim 1$, and thus, the corresponding exciton extension becomes isotropic with 1-ML coverage (see the Supplemental Material) [52]. Furthermore, E_{x} calculated within the GW-BSE formalism are in excellent agreement with those calculated using the hydrogenic model (Table I), which implies the applicability of this simplistic model to investigate excitons in such phosphorene derivatives with impurity coverage.

The SLPs with submonolayer coverages are both thermodynamically and kinetically stable. Further, the band edges align with the redox potentials for water-splitting reactions for SLPs with 0.33–0.5-ML oxygen/sulfur coverages [20]. Carrier effective masses in all directions are severely affected by the impurity coverage, and the resulting exciton binding energies are found to be high (see the Supplemental Material) [52]. The calculated E_{x} within the hydrogenic model is found to be 0.81 and 0.85 eV (0.85 and 0.86 eV) for 0.33- and 0.5-ML oxygen (sulfur) coverages. Such high exciton binding makes charge separation difficult in optoelectronic and catalytic devices. Thus, although the conduction and valence bands in these derivatives align with the redox potentials, the catalytic activity is expected to be negatively impacted due to high exciton binding. On the other hand, the high absorption coefficient [Figs. 2(c) and 2(d)] and robust exciton with high binding energy are desirable features for light-emitting device applications. In this regard, impurity-covered phosphorene can extend such application to green-light emission [69,70]. The anisotropy in exciton extension is in agreement with the analytical estimation of $\lambda \sim (\mu_x/\mu_y)^{1/3}$ and monotonically decreases with increasing coverage [52].

D. Exciton renormalization in few-layer and heterostructure phosphorene

While the layer-dependent evolution of gaps has been studied in few-layer phosphorene [49,64,71,72], it is intriguing to investigate the layer-dependent exciton binding. The effective screening increases with layer thickness, and in addition, the carrier masses along different crystallographic directions are also expected to be modified. The evolution in lattice parameters with increasing layer thickness agrees well with the previous prediction and converges to the bulk values (see the Supplemental Material) [49,52]. Further, the band gap in few-layer phosphorene decreases with thickness and converges to the value for black phosphorus [Fig. 3(b)]. The calculated bulk gap of 0.26 eV agrees reasonably well with the experimental measurement of 0.33 eV [73]. Considering the fact that the gaps are underestimated within the HSE06 functional, it is imperative to investigate its qualitative dependence on thickness. A power-law fit $E_g = aN_\ell^{-\alpha} + c$, with N_ℓ being the number of layers, indicates that E_g decays much slower (as $\alpha = 0.83$) than the usual quantum confinement with $\alpha = 2$. While $\alpha < 2$ is generic in weak van der Waals stacked two-dimensional materials, the calculated α in few-layer phosphorene is much smaller than that for MoS_2, for which $\alpha = 1.10$ [74].

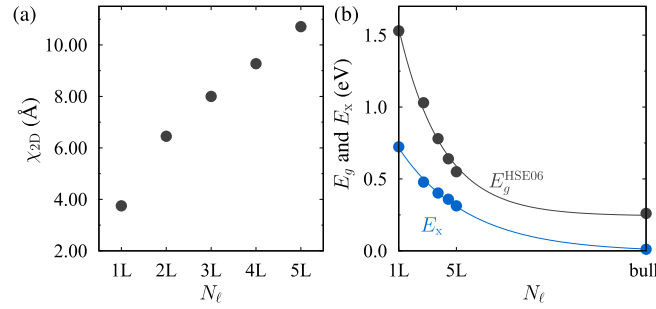

FIG. 3. (a) Calculated $\chi_{2D} = (\varepsilon - 1)L_v/4\pi$ increases with layer thickness N_ℓ, indicating an increase in electron screening. (b) The renormalization of band gap E_g and exciton binding E_x in few-layer phosphorene shows a power-law dependence with the layer thickness, and both quantities converge very slowly to the corresponding bulk value. The variation in exciton binding is largely determined by the effective hole mass m_h^* along the zigzag direction in addition to the change in effective electron screening.

The effective electron screening increases with thickness N_ℓ, and the static dielectric constant ε in few-layer phosphorene increases with the number of layers. The anisotropic ε in black phosphorus ($\varepsilon_x = 14.75$, $\varepsilon_y = 10.87$, $\varepsilon_z = 8.68$) are consistent with the experimental measurements of 16.5, 13, and 8.3 along the armchair, zigzag, and perpendicular directions, respectively [75]. The dependence of χ_{2D}, calculated using the average of anisotropic static ε, indicates increasing screening with thickness [Fig. 3(a)].

Effective carrier masses are mostly unaffected in few-layer phosphorene except for the hole mass along the zigzag direction, which exhibits a strong layer dependence (see the Supplemental Material) [52]. The calculated m_h^* along this direction decreases sharply with thickness N_ℓ, which is in agreement with a previous prediction [49]. To confirm the evolution of effective carrier masses with N_ℓ, we calculated the same for the bulk black phosphorus, which compares well with the experimental values (see the Supplemental Material) [52,76].

Consequently, the renormalization of exciton binding in few-layer phosphorene [Fig. 3(a)] is dictated by the strong dependence of the effective hole mass along the zigzag direction and the increase in effective screening with layer thickness. This result is in contrast to the assumption that the exciton binding and thus its variation are independent of carrier effective mass [6,77]. The large exciton binding sharply decreases from 0.72 eV in 1-ML phosphorene to 0.48 eV in 2-ML phosphorene and 0.31 eV in 5-ML phosphorene, which is still much higher than the corresponding

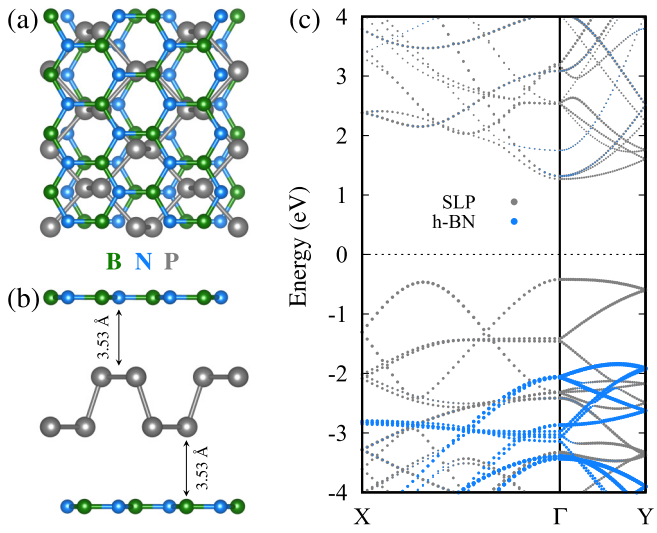

FIG. 4. (a) and (b) The top and side views of the h-BN/SLP/h-BN van der Waals encapsule. The structure is optimized using the PBE+D3-vdW functional with zero damping. The encapsulation induces a compressive (tensile) strain of 5.2% (1.3%) in the phosphorene layer along the armchair (zigzag) direction. (c) The valence band maxima and conduction band minima originate from the SLP and thus indicate a type-I band alignment. While the apparent band structure looks similar to the pristine SLP, the corresponding carrier effective masses are severely altered, which in turn modifies the exciton character.

bulk value. We estimated the Mott-Wannier exciton binding in black phosphorus $E_x^{3D} = (\mu/\varepsilon^2)R_\infty$ to be about 11 meV, which is much smaller than k_BT at room temperature and also much smaller than the same in bulk transition-metal dichalcogenides [13]. A similar power-law fit with $\alpha = 0.53$ indicates a much slower dependence of E_x on thickness than for E_g. Further, the exciton extension in few-layer phosphorene remains anisotropic, while the degree of anisotropy decreases (λ increases) monotonically with thickness (see the Supplemental Material) [52].

Black phosphorous is often encapsulated to avoid degradation and restore the intrinsic electronic properties [16,24,35]. Hexagonal boron nitride was demonstrated to be a good candidate material for this purpose [38–40]. Thus, it would be worth investigating how the electronic structure and effective dielectric screening are affected due to the substrate and capping. In this regard, we investigate the h-BN/SLP and h-BN/SLP/h-BN heterostructures [Figs. 4(a) and 4(b)]. To minimize the lattice strain in the phosphorene layer, we used a 1×3 supercell of phosphorene with an orthorhombic 1×4 cell of h-BN. Due to its puckered structure, the phosphorene lattice is relatively much softer than h-BN and can easily sustain a large strain. Thus, in relaxed geometry, the strain is induced in the phosphorene layer, while the h-BN lattice is mostly unaltered [52]. The band gap of SLP in these heterostructures is only slightly modified compared to the pristine case (see the Supplemental Material) [52]. We attribute this small change in the gap to the induced strain in the phosphorene layer in the heterostructure. These results are consistent with previous calculations [78,79].

Previously, the exciton binding energy was proposed to be independent of the effective mass [6]. In contrast, within the present model, E_x is determined by the effective mass and 2D polarizability. Moreover, the spatial anisotropic structure is directly related to the carrier effective masses, $\lambda \sim (\mu_x/\mu_y)^{1/3}$. Thus, in addition to the dielectric environment, any change in the intrinsic electronic structure in phosphorene due to the substrate and capping layer is important to consider for a correct description of the exciton. Indeed, the effective carrier mass in the phosphorene layer is affected by h-BN [52], which along with the electron screening from the h-BN layer reduces the exciton binding. The exciton binding is renormalized to 0.55 eV for the SLP/h-BN heterostructure, while the presence of a second h-BN layer in the h-BN/SLP/h-BN encapsulation does not alter the exciton binding further (0.53 eV). The excitons in these heterostructures are generated in the phosphorene layer, and no interlayer exciton is possible [Fig. 4(c)]. Further, the spatial anisotropy of excitons in these heterostructures is reduced [52]. Similar renormalization of exciton binding was predicted earlier for Al_2O_3/phosphorene/h-BN encapsulation and phosphorene on SiO_2 or PDMS substrates [77,80,81].

In this context, it should be noted here that both SLP/h-BN and h-BN/SLP/h-BN represent special cases of intralayer excitons owing to the band structure in Fig. 4(c), which is well described within the present model. Moreover, the present model can be extended to interlayer excitons, as was discussed previously for the MoS_2/h-BN/WSe_2 heterostructures [82].

IV. SUMMARY

We have studied the quasiparticle and optical properties of phosphorene and investigated the role of uniaxial strain and impurity coverages. The excitonic properties described within a tractable anisotropic hydrogenic model exhibit excellent agreement with those calculated by explicitly considering the electron-hole interaction within the GW-BSE formalism. In contrast to the previous assumption, the exciton binding strongly depends on effective carrier masses, which further determines the anisotropic spatial extension of excitons. Similar to the pristine SLP, excitons in strained and impurity-covered phosphorene remain strongly bound. However, the absorption edge, the corresponding dipole oscillator strength, and the anisotropy in spatial extension are severely altered. Owing to a severe alteration in the effective hole mass along the zigzag direction and increase in the electron screening, the exciton binding is greatly renormalized in few-layer phosphorene. In contrast, the exciton binding is relatively less affected in the h-BN and phosphorene heterostructures. The robust large exciton binding energy and tunable photoluminescence in encapsulated and impurity-covered phosphorene derivatives increase their prospective applications in light-emitting devices. Further, the results indicate that the present model will be applicable to other phosphorene-based superstructures and other two-dimensional anisotropic materials.

ACKNOWLEDGMENTS

We acknowledge the supercomputing facilities at the Centre for Development of Advanced Computing, Pune; Inter

University Accelerator Centre, Delhi; and the Center for Computational Materials Science, Institute of Materials Research, Tohoku University. M.K. acknowledges funding from the Department of Science and Technology through Nano Mission project SR/NM/TP-13/2016 and the Science and Engineering Research Board for the Ramanujan Fellowship.

[1] C. D. Spataru, S. Ismail-Beigi, L. X. Benedict, and S. G. Louie, Phys. Rev. Lett. **92**, 077402 (2004).
[2] L. Wirtz, A. Marini, and A. Rubio, Phys. Rev. Lett. **96**, 126104 (2006).
[3] F. Caruso, M. R. Filip, and F. Giustino, Phys. Rev. B **92**, 125134 (2015).
[4] J.-H. Choi, P. Cui, H. Lan, and Z. Zhang, Phys. Rev. Lett. **115**, 066403 (2015).
[5] P. Cudazzo, L. Sponza, C. Giorgetti, L. Reining, F. Sottile, and M. Gatti, Phys. Rev. Lett. **116**, 066803 (2016).
[6] T. Olsen, S. Latini, F. Rasmussen, and K. S. Thygesen, Phys. Rev. Lett. **116**, 056401 (2016).
[7] K. F. Mak and J. Shan, Nat. Photon. **10**, 216 (2016).
[8] L. Yang, M. L. Cohen, and S. G. Louie, Nano Lett. **7**, 3112 (2007).
[9] C. Zhang, A. Johnson, C.-L. Hsu, L.-J. Li, and C.-K. Shih, Nano Lett. **14**, 2443 (2014).
[10] H. M. Hill, A. F. Rigosi, C. Roquelet, A. Chernikov, T. C. Berkelbach, D. R. Reichman, M. S. Hybertsen, L. E. Brus, and T. F. Heinz, Nano Lett. **15**, 2992 (2015).
[11] A. R. Klots, A. K. M. Newaz, B. Wang, D. Prasai, H. Krzyzanowska, J. Lin, D. Caudel, N. J. Ghimire, J. Yan, B. L. Ivanov, K. A. Velizhanin, A. Burger, D. G. Mandrus, N. H. Tolk, S. T. Pantelides, and K. I. Bolotin, Sci. Rep. **4**, 6608 (2014).
[12] M. M. Ugeda, A. J. Bradley, S.-F. Shi, F. H. da Jornada, Y. Zhang, D. Y. Qiu, W. Ruan, S.-K. Mo, Z. Hussain, Z.-X. Shen, F. Wang, S. G. Louie, and M. F. Crommie, Nat. Mater. **13**, 1091 (2014).
[13] N. Saigal, V. Sugunakar, and S. Ghosh, Appl. Phys. Lett. **108**, 132105 (2016).
[14] D. Y. Qiu, F. H. da Jornada, and S. G. Louie, Phys. Rev. Lett. **111**, 216805 (2013).
[15] T. Byrnes, N. Y. Kim, and Y. Yamamoto, Nat. Phys. **10**, 803 (2014).
[16] L. Li, Y. Yu, G. J. Ye, Q. Ge, X. Ou, H. Wu, D. Feng, X. H. Chen, and Y. Zhang, Nat. Nanotechnol. **9**, 372 (2014).
[17] H. Liu, A. T. Neal, Z. Zhu, Z. Luo, X. Xu, D. Tománek, and P. D. Ye, ACS Nano **8**, 4033 (2014).
[18] R. Babar and M. Kabir, J. Phys. Chem. C **120**, 14991 (2016).
[19] A. Carvalho, M. Wang, X. Zhu, A. S. Rodin, H. Su, and A. H. Castro Neto, Nat. Rev. Mater. **1**, 16061 (2016).
[20] S. Arra, K. R. Ramya, R. Babar, and M. Kabir, J. Phys. Chem. C **122**, 7194 (2018).
[21] Q. Liu, X. Zhang, L. B. Abdalla, A. Fazzio, and A. Zunger, Nano Lett. **15**, 1222 (2015).
[22] J. Kim, S. S. Baik, S. H. Ryu, Y. Sohn, S. Park, B.-G. Park, J. Denlinger, Y. Yi, H. J. Choi, and K. S. Kim, Science **349**, 723 (2015).
[23] R. Babar and M. Kabir, Phys. Rev. B **97**, 045132 (2018).
[24] X. Wang, A. M. Jones, K. L. Seyler, V. Tran, Y. Jia, H. Zhao, H. Wang, L. Yang, X. Xu, and F. Xia, Nat. Nanotechnol. **10**, 517 (2015).
[25] G. Onida, L. Reining, and A. Rubio, Rev. Mod. Phys. **74**, 601 (2002).
[26] L. Hedin, Phys. Rev. **139**, A796 (1965).
[27] E. E. Salpeter and H. A. Bethe, Phys. Rev. **84**, 1232 (1951).
[28] S. Albrecht, L. Reining, R. Del Sole, and G. Onida, Phys. Rev. Lett. **80**, 4510 (1998).
[29] M. Rohlfing and S. G. Louie, Phys. Rev. Lett. **81**, 2312 (1998).
[30] L. Liang, J. Wang, W. Lin, B. G. Sumpter, V. Meunier, and M. Pan, Nano Lett. **14**, 6400 (2014).
[31] H. Shi, H. Pan, Y.-W. Zhang, and B. I. Yakobson, Phys. Rev. B **87**, 155304 (2013).
[32] A. Ramasubramaniam, Phys. Rev. B **86**, 115409 (2012).
[33] E. Prada, J. V. Alvarez, K. L. Narasimha-Acharya, F. J. Bailen, and J. J. Palacios, Phys. Rev. B **91**, 245421 (2015).
[34] L. Xu, M. Yang, S. J. Wang, and Y. P. Feng, Phys. Rev. B **95**, 235434 (2017).
[35] J. D. Wood, S. A. Wells, D. Jariwala, K.-S. Chen, E. Cho, V. K. Sangwan, X. Liu, L. J. Lauhon, T. J. Marks, and M. C. Hersam, Nano Lett. **14**, 6964 (2014).
[36] J. O. Island, G. A. Steele, H. S. J. van der Zant, and A. Castellanos-Gomez, 2D Mater. **2**, 011002 (2015).
[37] A. Favron, E. Gaufrès, F. Fossard, A.-L. Phaneuf-L'Heureux, N. Y.-W. Tang, P. L. Lévesque, A. Loiseau, R. Leonelli, S. Francoeur, and R. Martel, Nat. Mater. **14**, 826 (2015).
[38] A. Avsar, I. J. Vera-Marun, J. Y. Tan, K. Watanabe, T. Taniguchi, A. H. Castro Neto, and B. Özyilmaz, ACS Nano **9**, 4138 (2015).
[39] R. A. Doganov, E. C. T. O'Farrell, S. P. Koenig, Y. Yeo, A. Ziletti, A. Carvalho, D. K. Campbell, D. F. Coker, K. Watanabe, T. Taniguchi, A. H. Castro Neto, and B. Özyilmaz, Nat. Commun. **6**, 6647 (2015).
[40] X. Chen, Y. Wu, Z. Wu, Y. Han, S. Xu, L. Wang, W. Ye, T. Han, Y. He, Y. Cai, and N. Wang, Nat. Commun. **6**, 7315 (2015).
[41] G. Kresse and J. Hafner, Phys. Rev. B **47**, 558 (1993).
[42] G. Kresse and J. Furthmüller, Phys. Rev. B **54**, 11169 (1996).
[43] P. E. Blöchl, Phys. Rev. B **50**, 17953 (1994).
[44] J. P. Perdew, K. Burke, and M. Ernzerhof, Phys. Rev. Lett. **77**, 3865 (1996).
[45] H. J. Monkhorst and J. D. Pack, Phys. Rev. B **13**, 5188 (1976).
[46] M. Dion, H. Rydberg, E. Schröder, D. C. Langreth, and B. I. Lundqvist, Phys. Rev. Lett. **92**, 246401 (2004).
[47] G. Román-Pérez and J. M. Soler, Phys. Rev. Lett. **103**, 096102 (2009).
[48] S. Grimme, J. Antony, S. Ehrlich, and H. Krieg, J. Chem. Phys. **132**, 154104 (2010).
[49] J. Qiao, X. Kong, Z.-X. Hu, F. Yang, and W. Ji, Nat. Commun. **5**, 4475 (2014).
[50] A. Brown and S. Rundqvist, Acta Crystallogr. **19**, 684 (1965).
[51] L. Cartz, S. R. Srinivasa, R. J. Riedner, J. D. Jorgensen, and T. G. Worlton, J. Chem. Phys. **71**, 1718 (1979).
[52] See Supplemental Material at http://link.aps.org/supplemental/10.1103/PhysRevB.99.045432 for lattice parameter and band gaps in single and few-layered phosphorene, variation in

anisotropy and energy gap for uniaxially strained phosphorene, carrier mass for pristine as well as few-layer and impurity covered phosphorene, and structural, electronic and exciton properties of phosphorene-hBN heterostructure.

[53] M. Shishkin and G. Kresse, Phys. Rev. B **75**, 235102 (2007).

[54] M. Gajdoš, K. Hummer, G. Kresse, J. Furthmüller, and F. Bechstedt, Phys. Rev. B **73**, 045112 (2006).

[55] G. Strinati, Phys. Rev. B **29**, 5718 (1984).

[56] G. H. Wannier, Phys. Rev. **52**, 191 (1937).

[57] T. C. Berkelbach, M. S. Hybertsen, and D. R. Reichman, Phys. Rev. B **88**, 045318 (2013).

[58] A. Chernikov, T. C. Berkelbach, H. M. Hill, A. Rigosi, Y. Li, O. B. Aslan, D. R. Reichman, M. S. Hybertsen, and T. F. Heinz, Phys. Rev. Lett. **113**, 076802 (2014).

[59] L. V. Keldysh, JETP Lett. **29**, 658 (1979).

[60] P. Cudazzo, I. V. Tokatly, and A. Rubio, Phys. Rev. B **84**, 085406 (2011).

[61] J. Heyd, G. E. Scuseria, and M. Ernzerhof, J. Chem. Phys. **118**, 8207 (2003).

[62] A. V. Krukau, O. A. Vydrov, A. F. Izmaylov, and G. E. Scuseria, J. Chem. Phys. **125**, 224106 (2006).

[63] A. N. Rudenko and M. I. Katsnelson, Phys. Rev. B **89**, 201408 (2014).

[64] V. Tran, R. Soklaski, Y. Liang, and L. Yang, Phys. Rev. B **89**, 235319 (2014).

[65] X. Peng, Q. Wei, and A. Copple, Phys. Rev. B **90**, 085402 (2014).

[66] Z. Qiu, H. Fang, A. Carvalho, A. S. Rodin, Y. Liu, S. J. R. Tan, M. Telychko, P. Lv, J. Su, Y. Wang, A. H. Castro Neto, and J. Lu, Nano Lett. **17**, 6935 (2017).

[67] D. Çakır, H. Sahin, and F. M. Peeters, Phys. Rev. B **90**, 205421 (2014).

[68] B. Sa, Y.-L. Li, J. Qi, R. Ahuja, and Z. Sun, J. Phys. Chem. C **118**, 26560 (2014).

[69] J. S. Ross, P. Klement, A. M. Jones, N. J. Ghimire, J. Yan, D. G. Mandrus, T. Taniguchi, K. Watanabe, K. Kitamura, W. Yao, D. H. Cobden, and X. Xu, Nat. Nanotechnol. **9**, 268 (2014).

[70] F. Withers, O. Del Pozo-Zamudio, A. Mishchenko, A. P. Rooney, A. Gholinia, K. Watanabe, T. Taniguchi, S. J. Haigh, A. K. Geim, A. I. Tartakovskii, and K. S. Novoselov, Nat. Mater. **14**, 301 (2015).

[71] S. Zhang, J. Yang, R. Xu, F. Wang, W. Li, M. Ghufran, Y.-W. Zhang, Z. Yu, G. Zhang, Q. Qin, and Y. Lu, ACS Nano **8**, 9590 (2014).

[72] L. Li, J. Kim, C. Jin, G. J. Ye, D. Y. Qiu, F. H. da Jornada, Z. Shi, L. Chen, Z. Zhang, F. Yang, K. Watanabe, T. Taniguchi, W. Ren, S. G. Louie, X. H. Chen, Y. Zhang, and F. Wang, Nat. Nanotechnol. **12**, 21 (2016).

[73] Y. Akahama, S. Endo, and S.-i. Narita, J. Phys. Soc. Jpn. **52**, 2148 (1983).

[74] K. F. Mak, C. Lee, J. Hone, J. Shan, and T. F. Heinz, Phys. Rev. Lett. **105**, 136805 (2010).

[75] T. Nagahama, M. Kobayashi, Y. Akahama, S. Endo, and S.-i. Narita, J. Phys. Soc. Jpn. **54**, 2096 (1985).

[76] A. Morita, H. Asahina, C. Kaneta, and T. Sasaki, in *Proceedings of the 17th International Conference on the Physics of Semiconductors*, edited by J. D. Chadi and W. A. Harrison (Springer, New York, NY, 1985), pp. 1320–1324.

[77] G. Zhang, A. Chaves, S. Huang, F. Wang, Q. Xing, T. Low, and H. Yan, Sci. Adv. **4**, eaap9977 (2018).

[78] G. C. Constantinescu and N. D. M. Hine, Nano Lett. **16**, 2586 (2016).

[79] Y. Chen and S. Y. Quek, 2D Mater. **5**, 045031 (2018).

[80] D. Y. Qiu, F. H. da Jornada, and S. G. Louie, Nano Lett. **17**, 4706 (2017).

[81] A. Castellanos-Gomez, L. Vicarelli, E. Prada, J. O. Island, K. L. Narasimha-Acharya, S. I. Blanter, D. J. Groenendijk, M. Buscema, G. A. Steele, J. V. Alvarez, H. W. Zandbergen, J. J. Palacios, and H. S. J. van der Zant, 2D Mater. **1**, 025001 (2014).

[82] S. Latini, K. T. Winther, T. Olsen, and K. S. Thygesen, Nano Lett. **17**, 938 (2017).